1   **On the rapid manufacturing process of functional 3D printed sand molds**

2   Saptarshee MITRA[1], Antonio RODRÍGUEZ DE CASTRO[2], Mohamed EL MANSORI[1,3]

3

4   *[1]Laboratoire MSMP – EA7350, Arts et Métiers ParisTech, 2 Cours des Arts et Métiers,*

5   *13617Aix-en-Provence, France*

6   *[2]Laboratoire MSMP – EA7350, Arts et Métiers ParisTech, Rue Saint Dominique, 51006*

7   *Châlons-en-Champagne, France*

8   *[3]Texas A&M Engineering Experiment Station, College Station, TX 77843, USA*

9

10   **Abstract**

11

12   3D printing sand mold technology offers an opportunity for the foundry industry to rethink

13   old casting approaches and to revive the manufacturing approach using computer models. One

14   of the major concerns in sand molding using 3D printing is the functional characterization of

15   the 3D printed molds as its mechanical and mass transport properties. This research paper

16   discusses the effects of binder content on the mechanical strength and the permeability of 3DP

17   sand molds at different curing conditions. The local permeability of the 3DP specimen was

18   measured as a function of the injection flow rate in order to quantify the inertial pressure

19   effects. The mechanical strength of the 3DP sand molds was characterized using traditional

20   three-point bending strength measurements. The results show that the mechanical strength of

21   the printed molds is deeply dependent on the amount of binder and the curing process. The

22   3PB strength was found to increase when cured at 100 °C and decrease when cured at 200 °C

23 for all binder contents. The 3PB strength attains its maximum when cured at 100 °C for 2

24 hours for all binder content. In contrast, no significant effect of the amount of binder on the

25 initial permeability of the samples before curing was observed within the functional range of

26 binder mass fraction (1.02 to 1.98 %). Maximum permeability is attained at the same

27 conditions as the 3PB strength. Therefore, the mechanical strength of the sample can be

28 optimized within the investigated range of binder contents without resulting in any significant

29 decrease in permeability.

30

33

34 **1. Introduction**

35

36 Sand casting is a cost-effective method adopted in the production of metallic parts and is an

37 excellent solution to manufacture low-to-medium runs of parts meeting standard dimensional

38 requirements. Three-dimensional printing (3DP) of sand molds uses Powder Binder Jetting

39 (PBJ) technology and overcomes some of the issues commonly encountered in traditional

40 production methods. Indeed, 3DP technology allows rapid production of high-quality sand

41 molds with complex geometry as required in many casting applications [1,2], and ensures

42 optimized design freedom for any castable alloys [1–3]. The layer-based Three-Dimensional

43 Printing (3DP) technology is an Additive Manufacturing (AM) technique which was invented

44 at MIT to produce 3D parts directly from computer-aided designs (CAD) [4–7] This

45 technology has been fully recognized as one of the most promising technologies for the

46 production of casting sand molds. Among the available AM techniques, the powder-based

47 ink-jet 3D printing, which is based on the basis of a chemical reaction between silica sand

48 powder and an acidic binder, is widely used to manufacture sand molds. An extensive

49 literature review in this area of research [8] and a few studies on the relationship between the

50 properties of the 3D printed specimen and processing parameters [9,10] have been recently

51 published.

52

53 Foundries encounter a wide variation in the physical properties of the 3DP resin-bonded sand

54 molds, e.g. three-point bending (3PB) strength and permeability, which depend on certain

55 variables such as moisture and binder content. Indeed, greater binder contents generally result

56 in higher values of mechanical strength, but also in more gas being produced during metal

57 casting. Also, an excessively high amount of binder makes the 3DP sand mold too rigid

58 impeding proper expansion and giving rise to hot tearing defects and high residual stresses

59 [11,12]. In contrast, low binder amounts reduce the off-gassing but affect negatively the

60 mechanical strength, which can lead to penetration of the molten metal into the large inter-

61 sand interstices producing enlarged, rough surfaces on the casting. On the other hand, the

62 process of mold filling requires consideration of air evacuation from the mold cavity driven

63 by the compression of the gas by the melt. In particular, the melt can entrap air and other

64 gases in the mold cavity, which is favored by turbulent filling. Consequently, it is necessary to

65 evacuate the gas in an efficient manner in order to obtain a sound casting product with a

66 minimum of defects. For these reasons, the success of this novel technology is strongly

67 conditioned by the production of sufficiently permeable sand molds with convenient

68 mechanical strength for their manipulation.

69

70   3DP furan resin-bonded sand is widely used in casting due to the high dimensional precision

71   and mechanical strength of the produced parts. Furan Binder (FNB) is composed of an acid

72   catalyst (Toluene Sulfonic acid) and furfuryl alcohol which generates a 3-dimensional

73   polymer chain network (furan resin bridges) through acid-hardening reaction, polymerization,

74   and condensation. The polymer bridges (H-C bonds) observed in furan resin bonded sand

75   mold provide extra cohesion and strength to the silica sand particles, which is necessary in

76   order to retain the shape of 3D printed sand molds when in contact with the melt. The furan

77   binder condensation reaction produces water (dehydration), which tends to slow down the rate

78   of curing and hence affects the strength and permeability [13,14] of the molds. The recent

79   research shows that there are many possible factors affecting the quality of 3DP sand molds,

80   including furan resin binder content, curing temperature, curing time, types of base sand and

81   sand grain size [10,15–20]. All these works point out the high variability of the 3DP sand

82   molds.

83

84   The effects of curing time and temperature on permeability and mechanical strength using

85   ZCast 501 powder and Zb56 resin binder system of the ZCorporation were investigated by

86   other researchers [21]. The effects of curing time and temperature on permeability and

87   mechanical strength using ExOne 3D printed sand mold was also investigated [10], where it

88   was shown that the permeability decreased with increase in curing temperature. In the latter

89   work, a mathematical model was proposed to predict an optimal curing time and temperature

90   for both permeability and compressive strength. Also, the curing cycle of parts fabricated with

91   ZCAST® was optimized by taking into account the potential casting defects due to off-

92   gassing of volatile binder components [22,23]. These works showed that using higher

93   amounts of binder (8-9%) than the standard values in casting sand (1.4%) results in more off-

94   gassing and incomplete filling of the mold [8,22,23]. The same aspects were also studied in

95   the case of an ExOne^{TM} 3D printer, finding that the specimens had high mechanical strength

96   (~1.3 MPa) with less amount of binder than in ZCAST system, due to the well-controlled

97   distribution of silica sand and furan resin binder [23]. Recommendations on the orientation

98   and position of the samples in the job box can also be found in the recent literature in order to

99   minimize the anisotropic behavior of the molds produced with this technology [9].

100

101   ExOne S-Print is one of the latest machines for 3D printed porous sand molds using furan

102   binder system, and it requires curing (heat treatment) to remove the byproduct (water) from

103   the polycondensation (polymerization + condensation) of the furfuryl alcohol based

104   monomers (the furan resin), from the mold. This evolution of binder affects both the

105   mechanical and mass transport properties of the mold hence results in altered gas

106   permeability. In particular, the mass flow rate by which the air is evacuated from the molds is

107   directly related to pore size and binder percentage (microscopic characteristic length).

108   Therefore, there is a vital need for a suitable method for characterizing the permeability and

109   its relation to the curing temperature and time. The evolution of permeability and mechanical

110   strength of the 3DP sand molds during the curing stage was studied in a recent work using

111   traditional characterization methods for a unique value of binder content [10]. However, the

112   effects of binder content on permeability and 3PB strength have still not been studied to the

113   best of our knowledge. Such effects are expected to play a crucial role in the functionality of

114   the casted parts for the above-mentioned reasons. To fill this gap, the present study focuses on

115   the effect of binder mass fraction on permeability and mechanical strength of printed molds

116   for different curing temperatures and times.

117

118 **2. Theoretical background**

119

120 Three-point bending (3PB) tests are commonly used to characterize the mechanical strength

121 of brittle materials. These tests are comparatively easy to set up and interpret and are usually

122 performed on a rectangular bar, which is positioned over two roller pin supports while the

123 load is applied via a third roller pin typically mounted halfway between the pin supports. The

124 3PB bending stress is calculated using the measured load from Eq. 1:

125

$$\sigma = F \times \frac{3l}{2bd^2} \tag{1}$$

126 where F is the load at the middle section of the 3DP rectangular bar, l is the length between

127 the support span, b is the width of 3DP test bar and d is the thickness of the 3DP tested

128 sample.

129

130 Permeability can be defined as the ability of a porous medium to allow the fluids to pass

131 through it when driven by a pressure gradient. In the particular case of casting sands, the

132 standard method recommended by the American Foundry Society (AFS) consists in

133 determining gas permeability (GP), which is extensively used in foundry industries [24]. In

134 spite of the key advantages provided by the simplicity and rapidity of this traditional method,

135 GP is not an intrinsic porous-medium property and does not have permeability units [m^2].

136 Indeed, GP depends on the dynamic shear viscosity of the injected fluid, which increases with

137 temperature and generates higher pressure losses at higher temperatures for similar injection

138 flow rates. Also, the standard method does not take into account the inertial pressure drops

139   and compressibility of the fluid. Consequently, the obtained permeability value is not accurate

140   when the pressure gradient within the interstices of the sand is moderate or high. Furthermore,

141   usual GP characterization is frequently based on a unique-point measurement, so the result is

142   strongly influenced by experimental uncertainty. For these reasons, a rigorous method aiming

143   to improve the accuracy of permeability measurements in 3DP molds will be used in the

144   present work.

145

146   In the case of unconsolidated granular media as 3DP sand molds, permeability mainly

147   depends on the particle size distribution of the solids forming the bed, their shape, the liquid

148   saturation of the pore interstices and the packing structure (i.e. bed bulk porosity). When

149   dealing with casting processes, the pressure gradient is generated by the metallostatic pressure

150   during filling of the mold (to which an external pressure can be added) and the shrinkage of

151   the solidified alloy during cooling. Darcy's law (Eq. 2) is widely used to model the laminar

152   steady flow of Newtonian fluids through porous media (e.g. sand molds). This law relates the

153   volumetric flow rate to the pressure gradient through the viscosity of the fluid and the

154   permeability of the porous material.

155

$$\nabla P = \frac{\mu}{K} \frac{Q_v}{S} \qquad\qquad (2)$$

156   In the preceding equation, Q_v is the volumetric flow rate, S is the cross-sectional area, μ is the

157   dynamic shear viscosity of the injected fluid, $\nabla P = \frac{\Delta P}{L}$ is the pressure gradient and ΔP is the

158   pressure drop throughout a porous sample of length L and intrinsic permeability K. In

159   unidirectional flow, K is usually measured by injecting fluid with known viscosity through a

160   sample of the investigated medium of known dimensions. During the tests, either Q_v or ΔP is

161   imposed and the other magnitude is measured.

162

163   The value of K may be overestimated when performing measurements with gases at very low

164   flow rates in porous media with low permeability. This is caused by wall-slip of the gas flow

165   and is known as Klinkenberg effect [25,26]. Klinkenberg effect depends on the relative size of

166   the gas molecule with respect to the diameters of the pore, becoming significant only when

167   pore diameter is close to the mean free path of gas molecules. This is not the case of

168   commonly used casting sands, which exhibit high permeability levels. However, special

169   attention should be paid to the measurements performed at medium-to-high values of pressure

170   gradient, due to inertial effects which result in extra pressure losses that are not taken into

171   account by Darcy's law. Indeed, Darcy's law only applies to creeping flow in which inertial

172   forces are negligible compared to viscous forces [27–30]. Nonlinearity of fluid flow stems

173   from inertial pressure losses generated by the repeated accelerations and decelerations due to

174   rapid changes in flow velocity and direction along the flow path. Both theoretical and

175   empirical models taking into account the extra pressure losses due to inertial effects were

176   presented in the literature [31].

177

178   Forchheimer's empirical law [32] is commonly used to model the nonlinear behavior

179   associated to inertial regime through addition of a quadratic flow rate term to Darcy's law:

180

$$\nabla P = \frac{\Delta P}{L} = \frac{\mu}{K}\frac{Q_v}{S} + \rho\beta\left(\frac{Q_v}{S}\right)^2 \qquad (3)$$

181 with $\nabla P = \frac{\Delta P}{L} = \frac{P_i - P_o}{L}$, P_i being the absolute pressure at the inlet, P_o being the absolute

182 pressure at the outlet, ρ the density of the injected fluid and β the inertial coefficient.

183 Forchheimer's law has been experimentally validated and has found some theoretical

184 justifications [33–37].

185

186 The compressibility of the injected fluid is often neglected by the standard permeability

187 measurements used in casting. However, Q_v is not constant throughout the porous medium

188 when injecting compressible fluids, so Eq. 3 needs to be re-written in terms of mass flow rate

189 Q_m:

190

$$\bar{\rho}S\nabla P = \frac{\mu}{K}Q_m + \frac{\beta}{S}Q_m^2 \qquad (4)$$

191 where $\bar{\rho}$ is the average density of the fluid in the porous medium and $Q_m = \bar{\rho}Q_v$. For the sake

192 of simplicity, the left term of Eq. 4 will be named f ($f = \bar{\rho}S\nabla P$). If isothermal flow is assumed

193 and the compressible fluid is considered to be an ideal gas, the following relationship can be

194 used:

195

$$\frac{P}{\rho} = \frac{rT}{M} \qquad (5)$$

196   where P is the absolute pressure, T is the absolute temperature, r is the universal gas constant

197   ($\sim$ 8.31 J kg^{-1} mol^{-1}) and M is the molar mass of the gas ($\sim$ 28.96 g/mol for air). From Eq. 6,

198   it can be deduced that $Q_m \sim 1.29 \, Q_v$ for air flow when both Q_m and Q_v are given in SI units

199   and Q_v is taken as the volumetric flow rate in standard conditions of pressure and temperature.

200   From Eq. 5, $\bar{\rho}$ can be calculated as:

$$\bar{\rho} = \frac{M}{rT}\bar{P} = \frac{M}{rT}\frac{(P_i + P_o)}{2} \tag{6}$$

201   with $\bar{P}$ being the average pressure of the gas throughout the sample.

202

203   The criteria for transition from Darcian to non-Darcian flow regimes are commonly given in

204   terms of the non-dimensional Reynolds number Re. However, as discussed by researchers

205   [38], the definition of Re in granular unconsolidated porous media as casting sand is

206   controversial. This is due to the diverse characteristic lengths used in the definition of Re by

207   different authors: average grain size, pore constriction size, the square root of permeability,

208   etc. The latter authors showed that the use of Forchheimer number F_o is more suitable for

209   establishing the transition between creeping and inertial flows. F_o represents the ratio between

210   inertial and viscous pressure drops and is defined from Eq. 3 as follows:

211

212

$$F_o = \frac{\Delta P_{inertial}}{\Delta P_{viscous}} = \frac{\Delta P_{total} - \Delta P_{viscous}}{\Delta P_{viscous}} = \frac{\Delta P_{total}}{\frac{\mu Q_m L}{K\bar{\rho}S}} - 1 \tag{7}$$

213

214   According to researchers [38], the transition to non-Darcian flow occurs at $F_o = 0.11$ (10% of

215   inertial pressure drop), independently of the type of porous medium.

216

217   An apparent permeability K_{app} can be defined as follows for every couple of Q_m-ΔP

218   measurements:

219

$$K_{app} = \frac{\mu Q_m}{\rho S \nabla P} \tag{8}$$

220

221   The preceding definition can be derived from Eq. 8, by using $\beta = 0$. Therefore, the inertial

222   effects are not encompassed in K_{app} and it is expected to markedly differ from K at moderate

223   and high-pressure gradients. Standard permeability-characterization methods are based on the

224   measurement of K_{app}.This explains that these methods are extremely inaccurate unless the

225   flow rate used during the unique measurement is not meticulously selected, as will be shown

226   in subsection 4.3. Indeed, $K_{app} \sim K$ only at low flow rates ($F_o < 1$).

227

228   **3. Experimental setup and methods**

229

230   **3.1. Materials**

231

232 The raw materials used in the present experiments were quartz silica sand and a furfuryl-

233 alcohol-based binder (furan resin) of density (1.1-1.2) g/cm³. The silica sand grains had

234 regular spherical shape, with a mean diameter of 140 µm and a standard deviation of 25 µm,

235 which corresponds to American Foundry Society (AFS) size number 97. The furan binder was

236 a mixture of furfuryl alcohol (70-90 wt%), bisphenol A (5-15 wt%), resorcinol (1-10 wt%)

237 and 3-aminopropyltriethoxysilane (0.1-0.2 wt%) [39].

238

239 **3.2. Printing stage**

240

241 The specimens were first designed with the commercial software NetFabb[TM] [40], and were

242 then converted to .stl format. The bar specimens for 3 PB test were designed with length 172

243 mm, breadth 22.4 mm and height 22.4 mm. And the cylindrical specimens for permeability

244 test were designed with diameter = 35 mm and height 75 mm. The dimensions chosen were

245 according to the requirement by the machine for experimental testing of 3DP specimen.

246 Then, the samples were 3D-printed by means of an ExOne S-Print Furan machine [41], with a

247 job-box size of $800 \times 500 \times 400$ mm³. The printing process began by mixing sulfonic acid

248 (0.18 wt% of the sand) catalyst with 8 kg of silica sand grains inside the mixing chamber of

249 the 3D printer. The mixture was subsequently transferred to the re-coater. Successive layers of

250 280-µm thickness (i.e. 2 times the mean diameter of the sand grains) were spread over the

251 build platform and a compacting force was applied over the sand bed by means of a re-coater

252 head. Then, the print head nozzle injected the furfuryl alcohol binder on top of these sand

253 layers to bind them. As the droplets of furan resin binder were injected over the layer of acid-

254 activated silica sand bed, a coating layer was formed on top of each individual sand grain. The

255 surface of this resin-bonded sand grains crosslink with each other, forming a bridge of resin

256 binder between the sand particles formed by capillarity and gravitational forces immediately

257 after application of the binder. Then, and a hardening mechanism progressively occurs during

258 curing, making the sand particles bond closer as a result of surface tension and forming a

259 strong resin binder-particle bridge. The process continued until the last slice of the sample

260 was printed and the final two sand layers spread.

261

262 Previous experiments were performed to evaluate the effect of printing speed on the quality

263 and part integrity [42]. It was concluded that an increased printing speed would influence not

264 only the dimensional accuracy but also the mechanical strength of the 3DP parts due to

265 enhanced inertia forces. It is to be noted that a higher recoating speed also leads to non-

266 uniform spreading of sand over the job-box and low compaction of sand bed, generating

267 lower packing densities and high porosities. On the other hand, it is known that low recoating

268 speed leads to high sand packing density, and consequently to greater flexural strength [43].

269 The recommended process parameters for minimal variation in 3PB strength and permeability

270 along the job-box were selected according to Ref. [9,10,44] and are listed in Table 1. The

271 recoating speed was kept constant throughout the printing process and only the printing

272 resolution (furan drop spacing) was altered to achieve different binder percentages. It was

273 highlighted in previous works that loose sand does not provide a good support for the 3D

274 printed parts to build higher up in volume, and results in specimen sinking over the powder

275 bed during compaction [45–47]. Therefore, the specimens were printed over a thick sand layer

276 of 1.4 mm (around ten layers of sand) in order to avoid sinking, sub-layer displacements [45]

277 and sticking of the resin-bonded sand to the job-box.

278

279 A total of 180 (60 × 3 different binder content) cylindrical specimens were printed for

280 permeability tests. Also, 90 (30 × 3 different binder content) rectangular bars were printed for

281   the 3PB tests and (6 × 3 different binder content) 18 specimens were produced for loss on

282   ignition (LOI) tests. The initial dimensions of the 3D printed parts (bars) were measured using

283   a Vernier caliper, with length, breadth and height of 22.3 ± 0.02 mm, 22.2 ± 0.02 mm and

284   171.9 ± 0.07 mm, respectively (the uncertainty corresponds to 95% confidence interval). The

285   initial dimensions of the 3D printed parts (cylinders) were also measured using a Vernier

286   caliper, with length of 74.9 ± 0.01 mm and diameter of 34.8 ± 0.02 mm with 95% confidence

287   interval. The temperature of the printing room was 25 ± 3 °C and the relative humidity 40 ±

288   10%. After printing, the samples were then de-powdered, cleaned and taken out of the job-

289   box.

290

291   To go further, Scanning electron microscope (SEM) images were obtained using 3DP

292   specimens of 5mm in diameter and height, to verify the furan resin bridges between sand

293   particles. SEM images were obtained with a scanning electron microscope JEOL JSM-7001F.

294   Micrographs of 3DP samples were obtained in low vacuum (0 - 40 Pa) with an acceleration

295   voltage of 5 kV at a 100 μm working distance for different magnifications. The scans were

296   acquired and the obtained images were subsequently analyzed and processed using median

297   filter with the open-source platform for image analysis Fiji-ImageJ [48], in order to

298   differentiate between the sand particles, the pores, and the furan resin bridges. Samples of

299   SEM images are presented in Figure 1, showing the morphology of the furan resin bridges

300   within a cross-section of the 3D printed sample.

301

302

303   **3.3. Curing stages**

304

305 Despite providing superior mechanical strength to the 3DP parts, high binder amounts can

306 also generate a decrease in permeability, as the pores get filled with liquid. Also, more binder

307 leads to more off-gassing of the 3DP sand mold and the molds suffer from excessive moisture

308 generated from polycondensation reaction (dehydration) after printing. Therefore, samples

309 with usual mass fractions of binder require initial curing in order to remove excess moisture

310 content which affects their 3PB strength and permeability. For this reason, oven curing was

311 performed up to 60h at low temperatures to investigate its effect on the mechanical properties

312 of the 3DP mold [10]. The binder percentage was measured after this initial curing stage by

313 means of LOI test.

314

315 After the pre-curing stage 25 ºC, 100 °C and 200 °C were chosen as curing temperatures to

316 investigate the curing mechanisms. The choice of these temperatures is motivated by the

317 boiling points at room conditions of water and furfuryl alcohol, which are 100 °C and 180 °C,

318 respectively. Three curing times were considered: 0h, 2h, and 14h. Here the 0h conditions

319 represents the initial conditions of the specimen after printing. As observed in the previous

320 work [10], there is a rapid change in 3DP mold properties after 2h curing and approach a

321 constant value after 12h. Therefore, 0h, 2h, and 14h were chosen for the experiments. Images

322 of a set of heat-treated specimens are shown in Figure 2. One may note that the color of the

323 samples evolves during curing due to the progressive evaporation of binder and water. The

324 binder content, curing times and curing temperatures of the printed samples are listed in Table

325 2.

326

327 **3.4. Loss on Ignition tests**

328

329   The Loss-On-Ignition (LOI) test is used to measure the amount of volatile materials present in

330   a sample. In the case of the investigated 3DP sand samples, it was used to measure the mass

331   of binder, i.e. the combined mass of water, resin, catalyst, and volatile impurities. To do so,

332   the initial mass of the printed specimens was first measured, obtaining values close to 30g

333   (initial mass) in all cases. The specimens were then put into ceramic crucibles which had been

334   pre-heated at 100 °C for 1 h in an oven to extract moisture and organic residues. Once in the

335   crucibles, the 3DP specimens were heated at 900 °C for 45 min so as to burn-out and expel

336   the binder and moisture. After that, the crucible was removed from the oven and the mass of

337   the burnt-out specimen (final mass) was weighted. Images of the crucibles containing the

338   tested samples at the different stages of the LOI tests are provided in Figure 3. From the

339   results of the LOI, the binder contents of the samples were determined using Eq. 9:

340

$$\text{Binder content} = \frac{\text{initial mass} - \text{final mass}}{\text{initial mass}} \times 100 \ \% \qquad (9)$$

341

342   The remaining binder content at each stage of curing was calculated using this procedure, for

343   all curing temperatures and initial binder contents. 6 repetitions were performed for each

344   different binder specimens during the LOI test in order to estimate the experimental

345   uncertainty of the measurements.

346

347   **3.5. Porosity measurements**

348

349   The porosity of the samples was determined with the oven-dry method. The particle density

350   was considered as being the density of SiO_2-quartz (2648 kg.m^{-3}), which constitutes 99.1% of

351 the sand used by the printer. A laboratory precision balance was used to weight the printed

352 specimens after drying in a hot-air oven at 105 °C for 24 hours, and the bulk density of the

353 3DP specimen was calculated as the mass of sample per unit bulk volume. It is worth

354 reminding that both the volume of solid and the volume of pores were taken into account for

355 the calculation of bulk density. In contrast, the particle density was equal to the mass of

356 sample per unit volume of silica sand particles. From the bulk density and particle density, the

357 total porosity of the 3DP specimens was calculated as:

$$\text{Porosity} = 1 - \frac{\text{mass of the sample after LOI}}{\text{density of silica} \times \text{volume of the sample}} \tag{10}$$

358

359 The experimentally measured porosity values were close to 50% for all tested samples, with

360 an estimated standard deviation of 0.2%. 6 repetitions were performed with 6 analogous

361 specimens for each measurement in order to evaluate the uncertainty related to the

362 repeatability of the porosity tests.

363

364 **3.6. Three-Point bending tests**

365

366 The 3PB strength of the 3DP specimens was determined through destructive tests, as

367 commonly done with traditionally manufactured sand molds. The tests were performed using

368 a universal strength test machine (Simpson-Electrical PFG type) [49]. The bars were fixed to

369 the testing machine by means of two supporting pins separated 150 mm from each other. The

370 load was applied by a third pin at the mid-length of the 3DP bar, with a load rate of 0.1

371 MPa.s^{-1}, until the specimens broke. The maximum load capacity of the machine was 12.8

372 MPa and the uncertainty of the pressure gauge was ± 0.05 MPa. 4 repetitions were performed

373 with 4 analogous specimens for each measurement in order to assess uncertainty. For each

374 binder, the initial 3PB strength was measured using 4 distinct specimens. And the 0h

375 condition for each binder content specimen is same as of their initial 3PB strength for

376 different curing temperature.

377

378 **3.7. Permeability tests**

379

380 The permeability of the printed samples was measured using the experimental setup shown in

381 Figure 4, (Vinci Technologies^{TM} perm-meter [50]). The experimental procedure started by

382 inserting the cylindrical 3DP sample into a Viton sleeve and mounting it in a Hassler-type

383 core holder. After that, the core was confined with pressurized oil surrounding the sleeve in

384 order to avoid lateral leaks during flow. This oil was provided by an auxiliary confining pump

385 (Enerpac company). Then, air coming from a pressurized cylinder was continuously injected

386 through the cores at a controlled mass flow rate. A set of steeply increasing values of mass

387 flow rate was imposed by means of two mass flow rate regulators (Brooks Instrument B.V,

388 Accuracy: $\pm$ 0.7% of flow rate), with working ranges of 0 - 1 NL/min and $0 - 30$ NL/min,

389 respectively. The corresponding steady-state pressure drop ΔP between the inlet and the outlet

390 of the core (L = 75 mm) was measured by a membrane-type differential pressure sensor

391 (DP15 Variable Reluctance Pressure Sensor, Validyne Engineering, Accuracy: $\pm$ 0.2% of

392 flow rate). The outgoing air was released to atmospheric pressure, so P_o was assumed to be

393 0.1 MPa and $P_i = P_o + \Delta P$. Each measurement was repeated four times in order to evaluate

394 uncertainty related to the repeatability of the pressure. For each binder, the initial permeability

395 was measured using 4 distinct specimens at a low flow rate (0 - 1 NL/min) and 4 distinct

396 specimens at a high flow rate ($1 - 30$ NL/min). Therefore the 0h condition for each binder

397 content specimen is the same as of their initial permeability for different curing temperature.

398 A total of 10 flow rate (low flow rate + high flow rate) vs. pressure drop measurements were

399 performed for each case; covering the mass-flow-rate range from 0.01 Nl/min to 10 Nl/min.

400 The temperature of the core-holder was maintained at 23.0 ± 2 °C by using a temperature

401 control subsystem consisting of an electric heating thermostat. The dynamic shear viscosity of

402 air at this temperature was taken as 1.81×10^{-5} Pa s. 4 repetitions were performed with 4

403 analogous specimens for each measurement in order to evaluate the uncertainty related to the

404 repeatability of the tests.

405

406 **4. Results and discussion**

407

408 The effects of binder content on mass loss, permeability, and 3PB strength for uncured and

409 cured samples were experimentally investigated from the results of the measurements

410 presented in the preceding section.

411

412 **4.1. Evolution of binder content during curing as a function of the initial binder content**

413

414 The mass loss during curing, as measured by the LOI tests, are represented as a function of

415 curing time and temperature in Figure 5 for the three different values of binder content. All

416 the testing results were the mean value of six measurements. It is noted that loss of binder

417 mass by evaporation was negligible at the room temperature of 25 °C, even after 14h of

418 curing. This was expected given that 25 °C is far below the boiling temperatures of the water

419   and alcohols present in the binder. In contrast, a significant decrease in the mass of binder is

420   observed for the three initial values of binder content at both 100 °C and 200 °C. This

421   decrease is more pronounced within the first two hours of curing.

422

423   It is reminded that the furan binder (FNB) is a mixture of furfuryl alcohol and acid catalyst

424   [51]. FNB's condensation reaction produces water, which tends to slow down the rate of

425   curing (dehydration) affecting the mechanical properties of the 3DP mold [13,14]. A closer

426   look to Figure 5 reveals that the rate of mass loss when during curing at 200 °C is roughly

427   similar to the one at 100 °C, leading to analogous values of remaining binder content after 2h

428   and 12h in both cases. One may expect a higher evaporation rate at 200 °C, as this

429   temperature is greater than the boiling temperature of both alcohol and water. However, it

430   must be borne in mind that water is released only after polycondensation, which is

431   conditioned by the reaction of the acid catalyst with alcohol. Consequently, less water should

432   be released at 200 °C as the polycondensation reaction is interrupted by the early evaporation

433   of alcohol. Therefore, it can be concluded from Fig.8 that the mass of water being evaporated

434   at 100 °C is equivalent to the sum of the masses of water and alcohol being evaporated at 200

435   °C.

436

437   **4.2. 3PB strength as a function of the initial binder content for different curing**

438   **conditions**

439

440   Figure 6 shows the 3PB strength test results of 3DP sand specimens in the uncured and cured

441   conditions. All the testing results were the mean value of four measurements. It was found

442 that 3PB strength increases with binder content for all curing times and temperatures.

443 Moreover, 3PB strength increases when curing at 100 °C and decreases when cured at 200 °C

444 for all binder contents. When curing at 100°C, the 3PB strength experienced an increase of

445 20% for 1.02% binder, 16.7% for 1.46% binder and 28% for 1.98% binder. However, when

446 curing at 200 °C, the 3PB strength experienced a decrease of 41.6% for 1.02% binder, 40%

447 for 1.46% binder and 22% for 1.98% binder.

448

449 It is of crucial importance to manufacture 3DP sand molds meeting the requirements in terms

450 of gas evolution during metal casting (low binder content) and optimum 3PB strength. In this

451 regard, 3PB strength should be above 1.5 MPa so that the mold can resist the impact of liquid

452 metal. Therefore, 1.46 wt% of sand can be selected as the optimum furan resin binder content

453 to print 3DP molds for metal casting with the present technique. Indeed, when the initial furan

454 resin binder content is 1.46 wt%, the 2 h and 14 h strengths are above 2 MPa, satisfying

455 standard production requirement for casting melted alloy. It is also observed in Figure 6 that

456 3PB is unaltered by curing at 25 °C. The 3PB strength attains its maximum for all binder

457 content when curing at 100 °C for 2 hours. The reason is that the low roasting temperature

458 (100 °C) provides secondary hardening of furan resin bridges which increases the 3PB

459 strength, while the resin bonding bridges of 3DP sand mold burn at high curing temperature

460 (200 °C), resulting in reduced 3PB strength.

461

462 The 3PB strength of 3DP sand mold has a direct influence on the strength of the furan resin

463 bridge between sand grains in the sample (adhesion of binder between sand and cohesion of

464 the furan resin binder). This furan resin bridge is formed by capillary action after the binder is

465 dropped by the print head (X-resolution) and strengthens gradually. The intermolecular resin

466   bond strength depends on the physical state of the binder and its interaction with the

467   surrounding sand particles. When the 3DP specimen is cured, the furan resin binder hardens

468   by polycondensation (polymerization and condensation), forming a network furan resin

469   bridges which hold the sand particles together. The strength of the resin bridge greatly

470   depends on the amount of the binder content. The volume of the bridge corresponds to the

471   printed furan binder content minus the evaporated solvent (mixture water and alcohol). This

472   resin bridge strengthens gradually and affects the 3PB strength of the sample. The strength

473   increases more rapidly at 100 °C (cured by heat treatment) than at 25 °C (cured at room

474   temperature). However, this resin bridge hardening and strengthening mechanism have a

475   limit, leading to reduced strength and loss of ductility for prolonged heating at 100 °C or

476   when heating at high temperature (200 °C). These results facilitate the choice of the optimum

477   binder content, curing time and temperature to obtain the functional values of 3PB strength.

478

479   The mechanical and the mass transport properties of the cohesive granular materials depend

480   on their microscopic structure and their composition. A scheme of the resin-bonded bridges

481   between sand particles with simple cubic compaction density is displayed in Figure 7, where

482   R_{sand} is the radius of the silica sand particle and T_{binder} is the thickness of the furan resin

483   bridge. Considering that the binder is evenly distributed over the sand particles, the thickness

484   of the resin bridge is expected to increase when the binder content is increased. This leads to

485   improved cohesion strength of the bonding bridges and higher 3PB strength, in agreement

486   with the experimental results.

487

488   **4.3. Permeability as a function of the initial binder content for different curing**

489   **conditions**

490

491   The relationships between f ($= \bar{\rho} S \nabla P$) and Q_m obtained during permeability measurements for

492   uncured samples with different levels of initial binder content are shown in Figure 8. All the

493   testing results were the mean value of four measurements. It is noted that f increases

494   nonlinearly with increasing mass flow rate deviating from the linear relationship predicted by

495   Darcy's law (Eq. 3 with $\beta = 0$). As explained in section 2, Darcy's law is only valid for

496   creeping flow at low Reynolds numbers. Therefore, the non-linear behavior observed in

497   Figure 8 reveals that the flow is no longer creeping at moderate and high mass flow rates and

498   the inertial pressure losses are not negligible. The same figure shows that all f vs. Q_m curves

499   collapse for uncured samples, independently of the binder content. Therefore, similar values

500   of permeability and similar inertial pressure drops are expected for the three investigated

501   binder contents when curing is performed at room temperature (25 ℃). The f vs. Q_m

502   measurements for all the considered binder contents and curing conditions are represented in

503   Figure 9, showing that the curves also collapse for all curing conditions in the case of 1.02%

504   and 1.46% initial binder contents. Indeed, significant differences depending on the curing

505   time and temperature were only observed for 1.98% initial binder content, which will be

506   interpreted below in terms of permeability variation.

507

508   K_{app} was calculated using Eq. 8, as traditionally done with the standard permeability

509   characterization methods, for different values of the injection flow rate. The experimentally

510   obtained Q_m vs. K_{app} relationship for uncured samples with different binder contents is

511   presented in Figure 10. These results show that K_{app} is monotonically decreasing as Q_m

512   increases for all the specimens, which is explained by the inertial pressure drops which are not

513   taken into account in the calculation of K_{app}. Moreover, it is observed that the K_{app} tends to a

514   constant value within the low flow rates region in which the flow is viscous-dominated and

515   the inertial deviations are negligible. Therefore, $K_{app} \sim K$ at the lowest flow rates and K was

516   considered to be equal to the plateau value.

517

518   Darcy's law (Eq. 3 with $\beta = 0$) was then fitted to the f vs. Q_m measurements obtained during

519   permeability tests, as illustrated in Figure 11a for the uncured 1.02% binder content sample.

520   Similar results were observed for all considered curing conditions. From this figure, it can be

521   deduced that the flow regime is creeping only at the lowest flow rates in which Darcy's law

522   predictions are accurate. However, the deviations from Darcy's law become larger as Q_m is

523   increased due to additional inertial pressure drops. Therefore, it is confirmed that both

524   creeping and inertial flow regimes were covered by a wide range of Q_m imposed during the

525   measurements. Furthermore, F_o (Eq. 7) was also calculated as a function of Q_m so as to

526   quantify the relative importance of the inertial pressure drops, as presented in Figure 11b. The

527   critical value of $F_o = 0.11$ (10% of inertial pressure drop) marking the transition from

528   Darcian to non-Darcian flow occurs at Q_m close to 3×10^{-6} kg/s. Accordingly, for the given

529   sample dimensions and experimental conditions, it can be concluded that flow rates close to 3

530    $\times 10^{-6}$ kg/s must be used to characterize permeability in this type of casting sands. Non-

531   dimensionalization of this criterion is challenging given the compressibility of the injected

532   fluid and will not be addressed in the present work.

533

534   Following the procedure presented above, the permeability of the samples was calculated for

535   all the investigated binder contents, curing times and temperatures. The results are presented

536   in Figure 12. It can be observed that no significant evolution of K over time was obtained for

537   the samples cured at 25 ℃. This was expected, given the low evaporation rate at room

538   temperature in agreement with previous results [21] and the mass loss measurements

539   presented in Fig. 5. Moreover, the permeability of these samples is very close for all binder

540   contents. This may be explained by the combined effect of two mechanisms with opposed

541   effects on permeability: 1) the generation of thicker resin bridges through polymerization at

542   higher binder amounts tend to separate of the grains, which enhances porosity and

543   permeability; and 2) higher binder amounts lead to a higher saturation of the interstices,

544   resulting in a decrease in permeability. However, these mechanisms need further verification,

545   for example through specifically dedicated X-ray micro-computed tomography (µ-CT)

546   experiments, which will not be presented here.

547

548   It can also be observed in Figure 12 that the permeability of the 1.02% binder content samples

549   remains roughly constant throughout the 14h of curing at the three considered temperatures.

550   This may be explained by the thinness of the liquid layer between the sand grains which

551   produces only a very weak reduction in permeability. Also, the polymerization reaction

552   (transformation of the liquid binder into resin bridges) is expected to conclude earlier than for

553   higher amounts of binder, so the liquid saturation is lower and the effects of remaining

554   alcohol and water evaporation are minimum. A stronger effect of evaporation on permeability

555   is observed at 1.46% and 1.98% binder contents, which is potentially due to the higher

556   amount of remaining alcohol and water blocking air flow through the pores. Also, a decrease

557   in permeability is observed after 14h of curing, which could be explained by the shrinkage

558   effect produced by the burning of the resin bridges [52]. The permeability attains its

559   maximum in the case of the specimen with the highest binder content when heat-treated at

560   100°C for 2h. It is to be noted that higher amounts of binder would generate more toxic gas.

561

5. Conclusion

The quality of the parts produced by casting in 3DP molds is strongly conditioned by the careful choice of suitable binder content. Motivated by the vital role of this process parameter, the effects of binder content on the permeability and the mechanical strength of 3DP sand molds has been experimentally evaluated for different curing times and temperatures. The following conclusions are drawn from the present work:

- ✓ Binder content has a profound influence on the 3PB strength of 3DP sand molds. Higher binder amounts lead to increased mechanical strengths. Moderate curing temperatures and times (100 ºC, 2h) are recommended in order to optimize 3PB (avoiding degradation of the resin bridges, excessive off-gassing, and hot tearing).
- ✓ Mass-loss measurements performed during LOI tests allow the evaluation of liquid evaporation rates, which can be subsequently used in the analysis of the physical mechanisms governing the changes in permeability and 3PB strength during the curing stage.
- ✓ The effect of binder content on permeability is not significant when curing at room temperature (25 ºC). However, liquid evaporation and binder shrinkage significantly affect permeability. Maximum permeability is attained at the same conditions as the optimum 3PB strength.
- ✓ The porosity of the 3DP sand molds is very high, leading to inertial-dominated flows at moderate values of air flow rate. Consequently, permeability measurements must be performed at sufficiently low injection flow rates in order to achieve creeping flow.

586   The present experimental results facilitate the characterization of printing process parameters

587   by quantifying the effects of binder content on the functionality of 3DP molds. These criteria

588   are most valuable for the production of casting molds meeting the requirements of aerospace

589   and automotive industries.

590

591 **6. Acknowledgements**

592

597

598

599

600

601   **References**

602

603   [1]   Almaghariz ES, Conner BP, Lenner L, Gullapalli R, Manogharan GP, Lamoncha B, et

604   al. Quantifying the role of part design complexity in using 3d sand printing for molds

605   and cores. Int J Met 2016;10:240–52. doi:10.1007/s40962-016-0027-5.

606   [2]   Almaghariz ES. Determining When to Use 3D Sand Printing : Quantifying the Role of

607   Complexity By Eyad S . Almaghariz A thesis Submitted in Partial Fulfillment of the

608   Requirements for the Degree of Master of Science in the 2015.

609   [3]   Conner BP, Manogharan GP, Martof AN, Rodomsky LM, Rodomsky CM, Jordan DC,

610   et al. Making sense of 3-D printing: Creating a map of additive manufacturing products

611   and services. Addit Manuf 2014;1:64–76. doi:10.1016/j.addma.2014.08.005.

612   [4]   Sachs E, Cima M, Cornie J, Bredt J, Fan A, Lee K, et al. Dimensional Printing: Rapid

613   Tooling and Prototypes Directly from CAD Representation. Solid Free Fabr Symp

614   1990:27–47. doi:10.1016/S0007-8506(07)61035-X.

615   [5]   Sachs E, Cima M, Cornie J, Brancazio D, Bredt J, Curodeau A, et al. Three-

616   Dimensional Printing: The Physics and Implications of Additive Manufacturing. CIRP

617   Ann - Manuf Technol 1993;42:257–60. doi:10.1016/S0007-8506(07)62438-X.

618   [6]   Bredt JF, Anderson T. Method of three dimensional printing, 1999.

619   [7]   Williams CB. Design and development of layer-based additive manufacturing process

620   for realization of metal parts of designed mesostructure 2008:421.

621   [8]   Upadhyay M, Sivarupan T, El Mansori M. 3D Printing for Rapid Sand Casting - A

622   Review. J Manuf Process 2017;29:211–20. doi:10.1016/j.jmapro.2017.07.017.

623   [9]   Coniglio N, Sivarupan T, El Mansori M. Investigation of process parameter effect on

624   anisotropic properties of 3D printed sand molds. Int J Adv Manuf Technol 2017:1–11.

625   doi:10.1007/s00170-017-0861-5.

626   [10]   Mitra S, Rodríguez de Castro A, El Mansori M. The effect of ageing process on three-

627   point bending strength and permeability of 3D printed sand molds. Int J Adv Manuf

628   Technol 2018;97:1241–51. doi:10.1007/s00170-018-2024-8.

629   [11]   Marumoto N, Kashimura H, Yoshida K, Toyoda T, Okane T, Yoshida M. Dynamic

630   measurements of the load on gray cast iron castings and contraction of castings during

631   cooling in furan sand molds. J Mater Process Technol 2016;237:48–54.

632   doi:10.1016/j.jmatprotec.2016.05.012.

633   [12]   Motoyama Y, Inoue Y, Saito G, Yoshida M. A verification of the thermal stress

634   analysis, including the furan sand mold, used to predict the thermal stress in castings. J

635   Mater Process Technol 2013;213:2270–7. doi:10.1016/j.jmatprotec.2013.06.024.

636   [13]   Zeitsch KJJ. The Chemistry and Technology of Furfural and its Many By Products.

637   vol. 13. 2001. doi:10.1016/S1385-8947(00)00182-0.

638   [14]   Quaker T, Company O. Catalyst composition and method for curing furan-based

639   foundry binders-US 4451577 A 1984.

640   [15]   Chang KK, Hutchings DA. Furan no-bake foundry binders and their use. 6593397,

641   2002.

642   [16]   Wan P, Li LC, Zhang L, Wang WQ. Research on testing method of resin sand high

643   temperature compressive strength. China Foundry 2016;13:335–41.

644   doi:10.1007/s41230-016-6013-y.

645 [17] Surekha B, Rao DH, Rao GKM, Vundavilli PR. Design and Development of

646   Knowledge Base Scheme for Chromite-based Resin Bonded Sand Core System.

647   Procedia Mater Sci 2014;6:919–25. doi:10.1016/j.mspro.2014.07.161.

648 [18] Khandelwal H, Ravi B. Effect of Binder Composition on the Shrinkage of Chemically

649   Bonded Sand Cores. Mater Manuf Process 2015;30:1465–70.

650   doi:10.1080/10426914.2014.994779.

651 [19] Khandelwal H, Ravi B. Effect of molding parameters on chemically bonded sand mold

652   properties. J Manuf Process 2016;22:127–33. doi:10.1016/j.jmapro.2016.03.007.

653 [20] Liu F, Yang L, Huang Y, Jiang P, Li G, Jiang W, et al. Performance of resin bonded

654   sand for magnesium alloy casting. J Manuf Process 2017;30:313–9.

655   doi:10.1016/j.jmapro.2017.10.002.

656 [21] Mckenna N, Singamneni S, Diegel O, Singh D, Neitzert T, George JS, et al. Direct

657   Metal casting through 3D printing : A critical analysis of the mould characteristics. 9th

658   Glob Congr Manuf Manag 2008:12–4.

659 [22] Snelling D, Kay R, Druschitz A, Williams CB. Mitigating Gas Defects in Castings

660   Produced From 3D Printed Molds. 117th Met. Congr., 2013.

661 [23] Snelling D, Williams CB, Druschitz AP. A Comparison of Binder Burnout and

662   Mechanical Characteristics of Printed and Chemically Bonded Sand Molds. SFF Symp

663   2014:197–209.

664 [24] Simpson. Simpson Permeability Meter PDU-D. vol. 41. 2002.

665 [25] Klinkenberg LJ. The Permeability of Porous Media To Liquids and Gases. Drilling and

666   Production Practice, New York, 1 January 1941, API-41-200 n.d.

667   [26]   Tanikawa W, Shimamoto T. Klinkenberg effect for gas permeability and its

668   comparison to water permeability for porous sedimentary rocks. Hydrol Earth Syst Sci

669   Discuss 2006;3:1315–38. doi:10.5194/hessd-3-1315-2006.

670   [27]   Hubbert MK. Darcy's law and the field equations of the flow of underground fluids.

671   vol. 2. 1957. doi:10.1080/02626665709493062.

672   [28]   Schneebeli G. Expériences sur la limite de validité de la loi de Darcy et l'apparition de

673   la turbulence dans un écoulement de filtration. La Houille Blanche 1955:141–9.

674   doi:10.1051/lhb/1955030.

675   [29]   Scheidegger AE. The physics of flow through porous media 1957:236 p.

676   [30]   Chauveteau G, Thirriot CL. Régimes d'écoulement en milieu poreux et limite de la loi

677   de Darcy. La Houille Blanche 1967;2:141–8. doi:10.1051/lhb/1967009.

678   [31]   Miskimins JL, Lopez, H J, Baree RD. Non-Darcy Flow in Hydraulic Fractures: Does It

679   Really Matter? SPE Annu. Tech. Conf. Exhib., Dallas,Texas: Society of Petroleum

680   Engineers; 2005, p. 8.

681   [32]   Forchheimer P. Wasserbewegung durch Boden [Movement of Water through Soil].

682   Zeitschrift Des Vereins Dtsch Ingenieure 1901;45:1782–8.

683   [33]   Dullien FAL, Azzam MIS. Flow rate-pressure gradient measurements in periodically

684   nonuniform capillary tubes. AIChE J 1973;19:222–9. doi:10.1002/aic.690190204.

685   [34]   Geertsma J. Estimating the Coefficient of Inertial Resistance in Fluid Flow Through

686   Porous Media. Soc Pet Eng J 1974;14:445–50.

687   [35]   Macdonald IF, El-Sayed MS, Mow K, Dullien FAL. Flow through Porous Media-the

688   Ergun Equation Revisited. Ind Eng Chem Fundam 1979;18:199–208.

689   doi:10.1021/i160071a001.

690   [36]   Rasoloarijaona M, Auriault JL. Nonlinear seepage flow through a rigid porous

691   medium. Eur J Mech - B/Fluids 1991;13:177–95.

692   [37]   Javadi M, Sharifzadeh M, Shahriar K, Mitani Y. Critical Reynolds number for

693   nonlinear flow through rough-walled fractures: The role of shear processes. Water

694   Resour Res 2014;50:1789–804. doi:10.1002/2013WR014610.

695   [38]   Zeng Z, Grigg R. A Criterion for Non-Darcy Flow in Porous Media. Transp Porous

696   Media 2006;63:57–69. doi:10.1007/s11242-005-2720-3.

697   [39]   ExOne. FB001 (Furan Binder) - Fiche De Données De Sécurité Caprolactam,selon

698   1907/2006/CE, Article 31 2014:2–11.

699   [40]   Autodesk Inc. Netfabb® 2017.

700   [41]   ExOne. S-Print [TM] Furan. 2014.

701   [42]   Miyanaji H, Momenzadeh N, Yang L. Effect of printing speed on quality of printed

702   parts in Binder Jetting Process. Addit Manuf 2018;20:1–10.

703   doi:10.1016/j.addma.2017.12.008.

704   [43]   Bobby SS. A Preliminary Investigation of Gypsum Bonded Moulds By Three

705   Dimensional Printing. IJRET Int J Res Eng Technol 2014;03:501–7.

706   [44]   Sivarupan T, ElMansori M, Coniglio N. 3D Printing Process Parameters and Properties

707   of Additively Manufactured Sand Mold for Rapid Casting : Strength and Permeability.

708   Addit Manuf 2017:(under review).

709   [45]   Lee JJ, Sachs E, Cima M. Layer position accuracy in powder based rapid prototyping.

710   Rapid Prototyp J 1995;1:24–37. doi:10.1108/13552549510104447.

711   [46]   Dimitrov D, Beer N. Developing capability profile for the three dimensional printing

712   process. R D J 2006;22:17–25.

713   [47]   D.M. Dimitrov, N. de Beer. IMPROVEMENTS IN THE CAPABILITY PROFILE OF

714   3-D PRINTING: AN UPDATE. South African J Ind Eng 2014;25:1–12.

715   doi:10.11842/wst.2014.02.015.

716   [48]   Schindelin J, Arganda-Carreras I, Frise E, Kaynig V, Longair M, Pietzsch T, et al. Fiji:

717   An open-source platform for biological-image analysis. Nat Methods 2012;9:676–82.

718   doi:10.1038/nmeth.2019.

719   [49]   Simpson. SIMPSON Universal Strength Machine PFG. vol. 41. 2008.

720   [50]   Vinci Technologies. BENCH TOP PERMEAMETER SYSTEM n.d.

721   [51]   Holtzer M, Dańko R. Molds and Cores Systems in Foundry 2015:27–43.

722   doi:10.1007/978-3-319-14583-9.

723   [52]   Lowe K E, Showman R E. Dimensional Changes in Chemically Bonded Molds and

724   Cores. Trans Am Foundry Soc 2011;119:251–60.

725

726

727

728

729

730

731

732
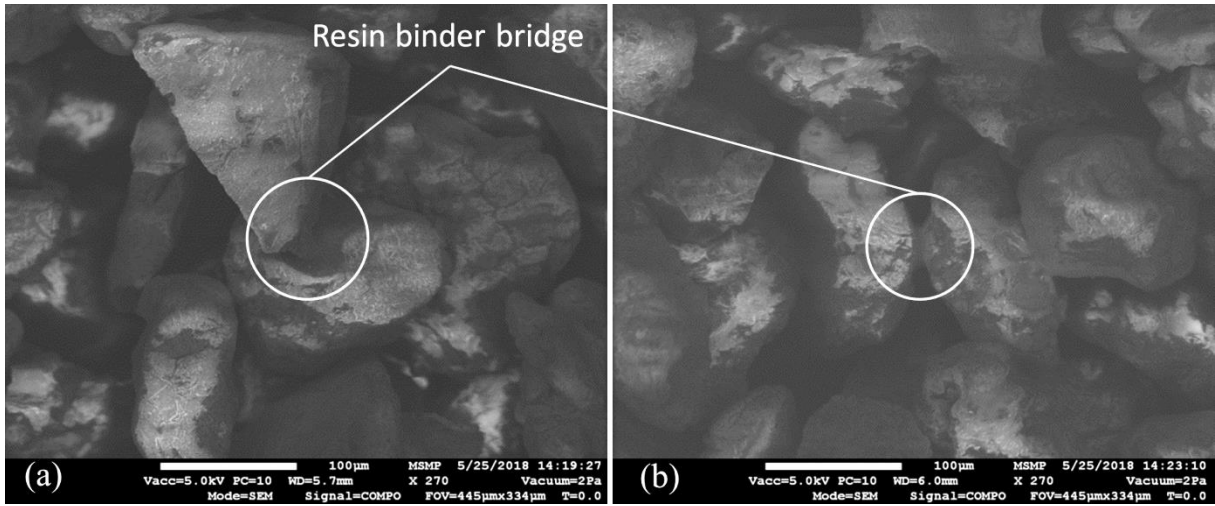
Figure 1. Scanning electron microscope (SEM) image of the 3DP sample, (a, b) zoom

showing the resin bridges

735

736

737
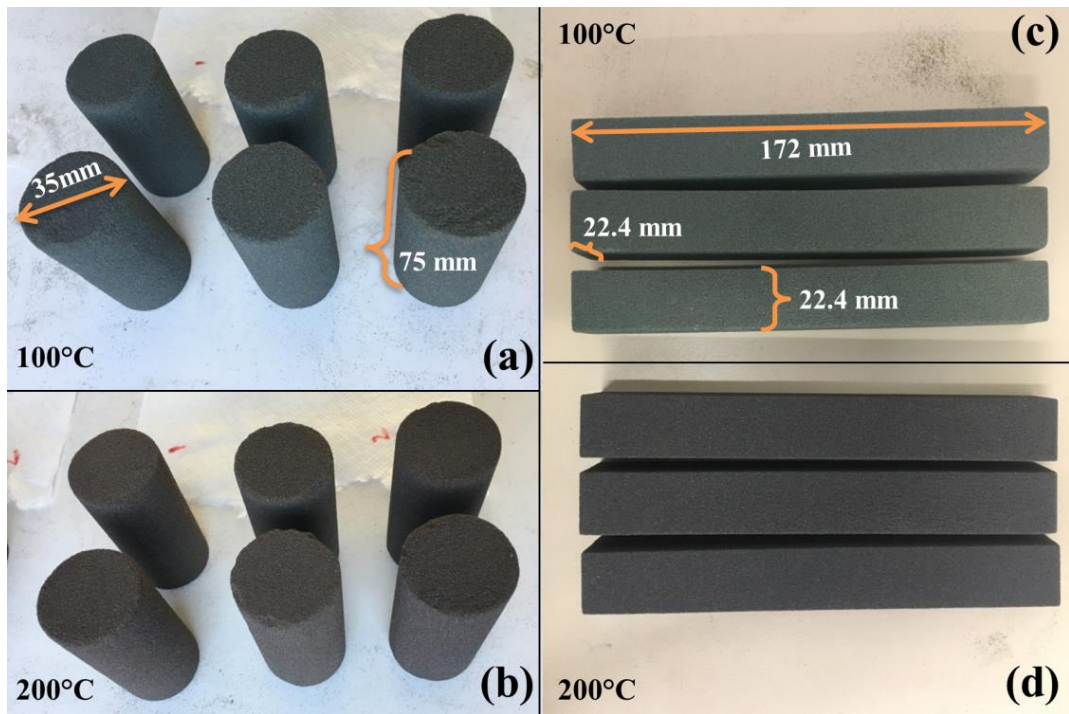
Figure 2. Heat-treated 3DP samples with 1.45% binder, (a,b) cylinders and (c,d) bars

739

740

741 **Figure 3:** LOI test with (a) 3DP specimens, (b) immediately after taking out of the oven at
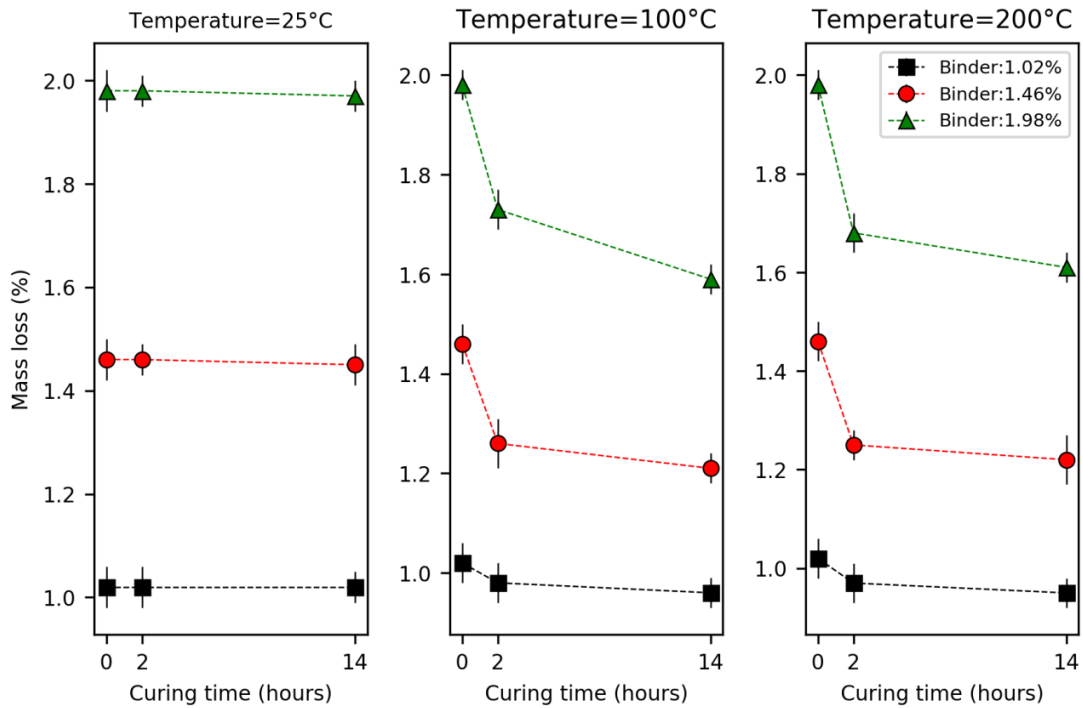
742 900 °C

743

744
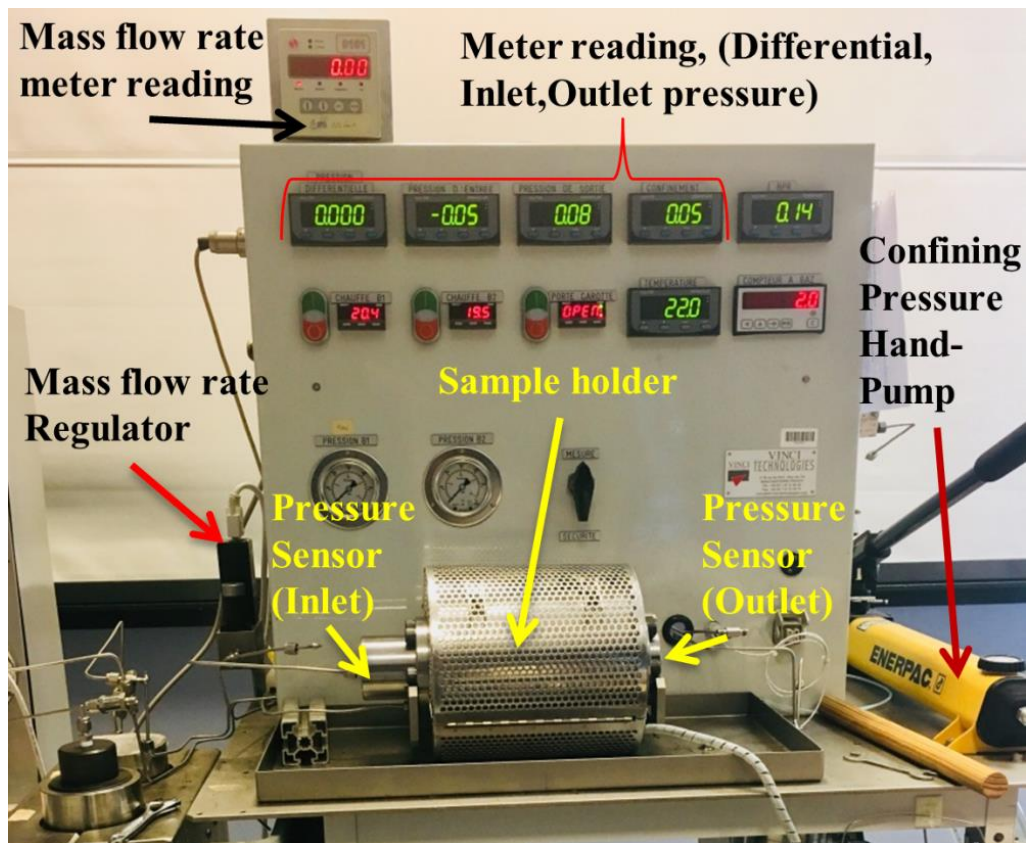
745
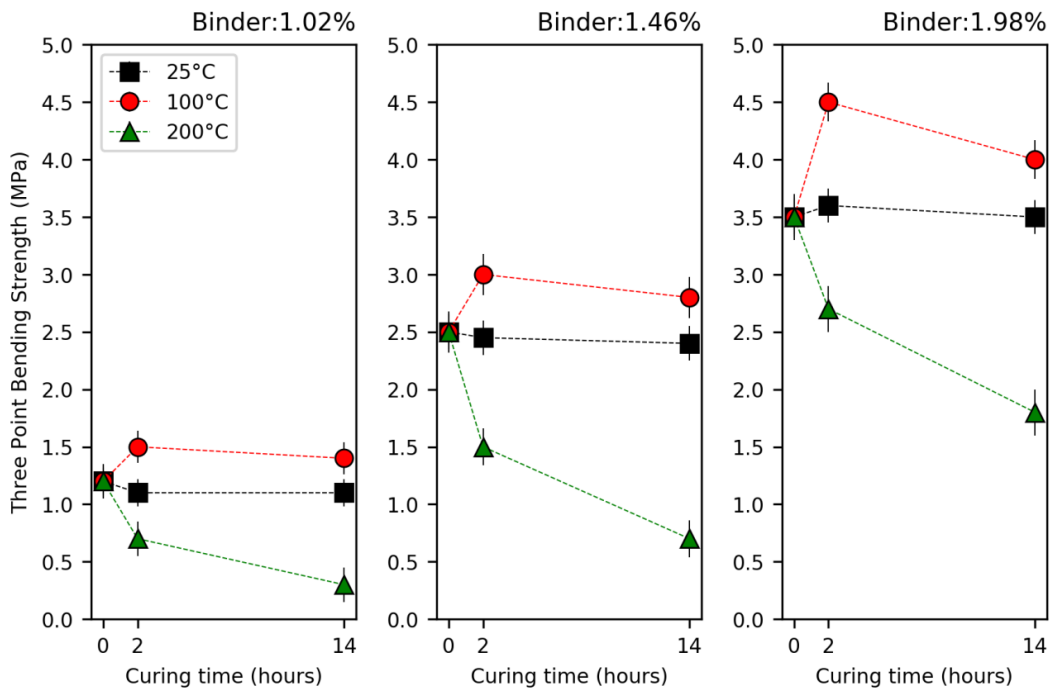
746 **Figure 4.** Perm-meter setup

747

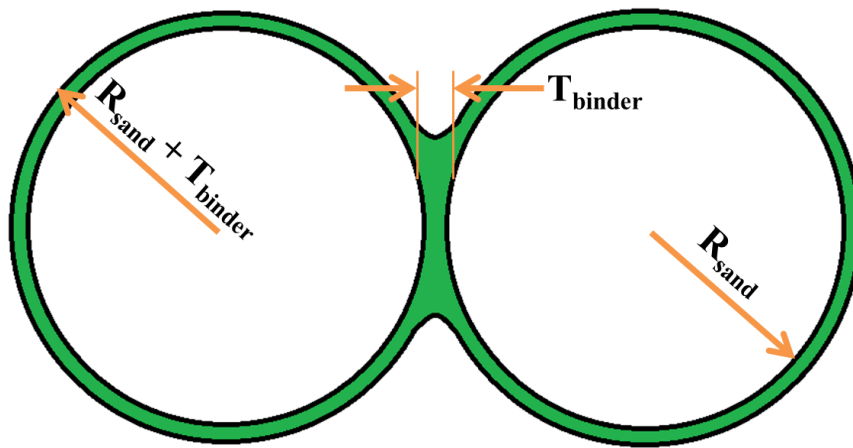**Figure 5.** Mass loss as a function of curing time for three curing temperatures

749

750

Figure 6. Effect of curing parameters on 3PB strength

751

752

753

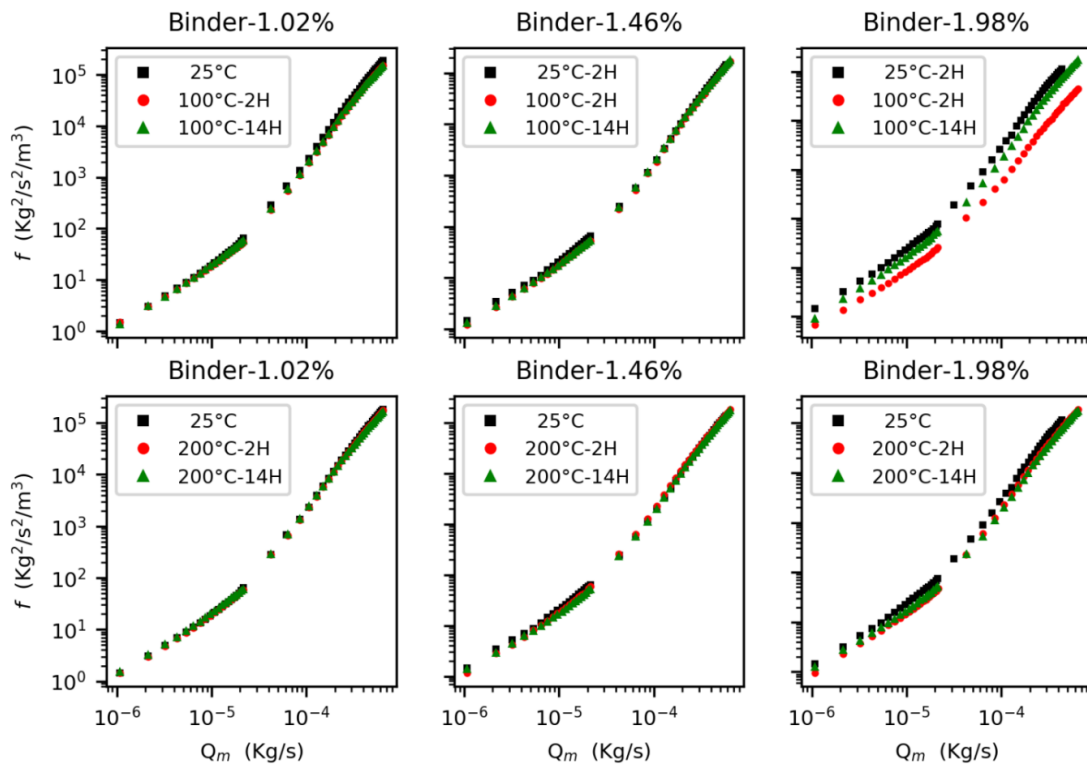754 **Figure 7.** Resin bonding bridge of adjacent sand particles

755
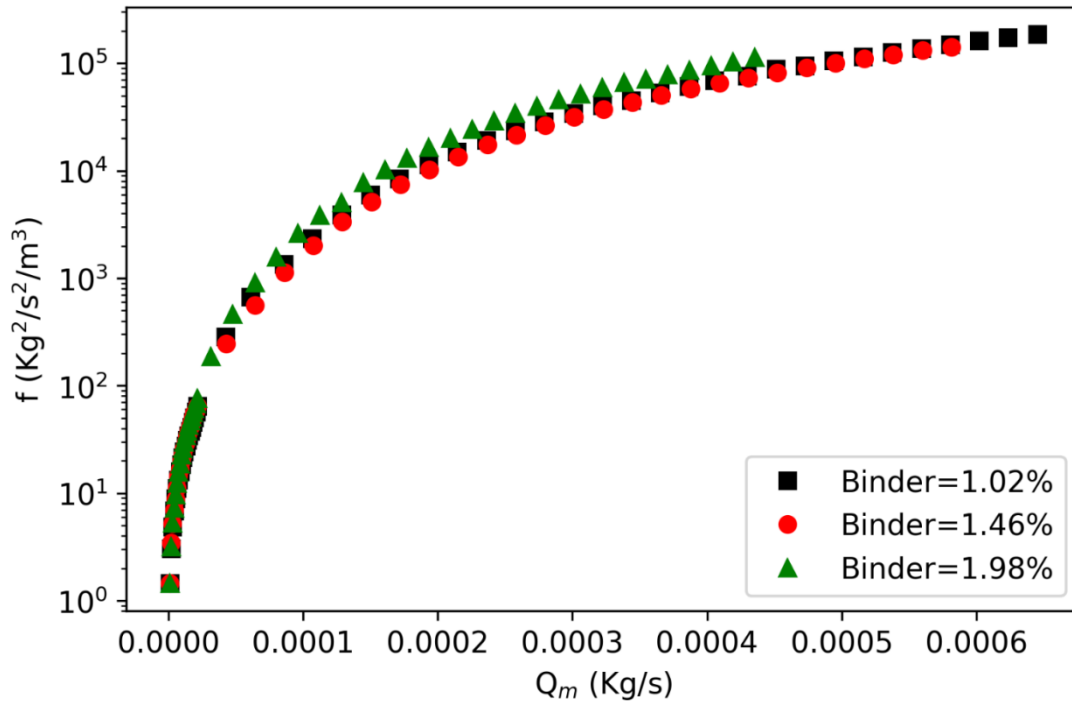
756

757

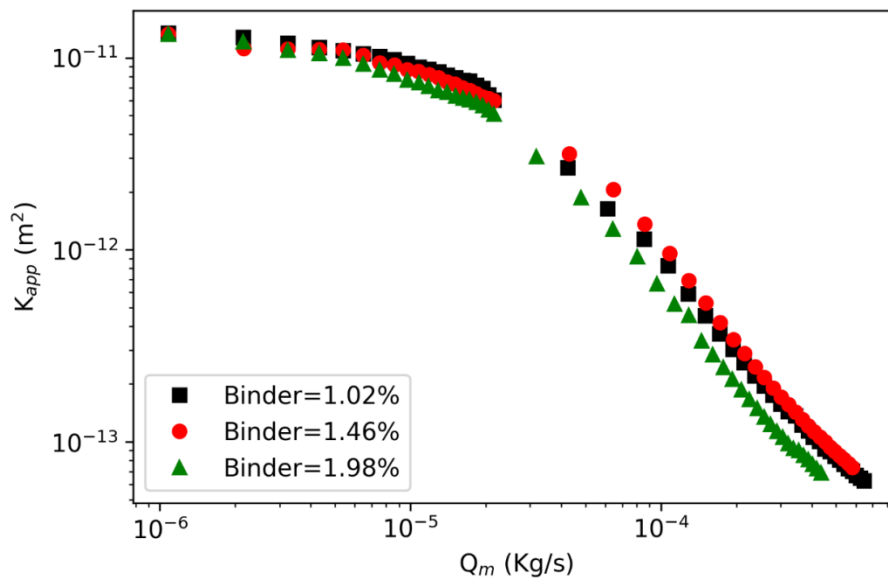758 **Figure 8.** Effect of binder content on f vs. Q_m rate for uncured samples at 25°C.

759

Figure 9. Effect of curing time on the relationship between f and Q_m at different temperatures
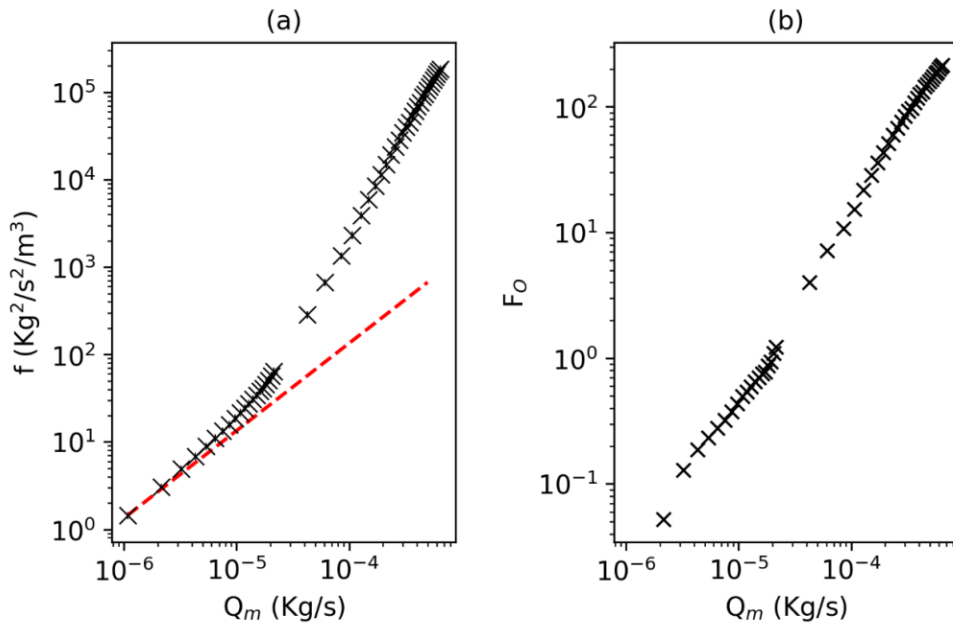
760

761 and binder contents

762

763

Figure 10. Relationship between apparent permeability and mass flow rate for uncured
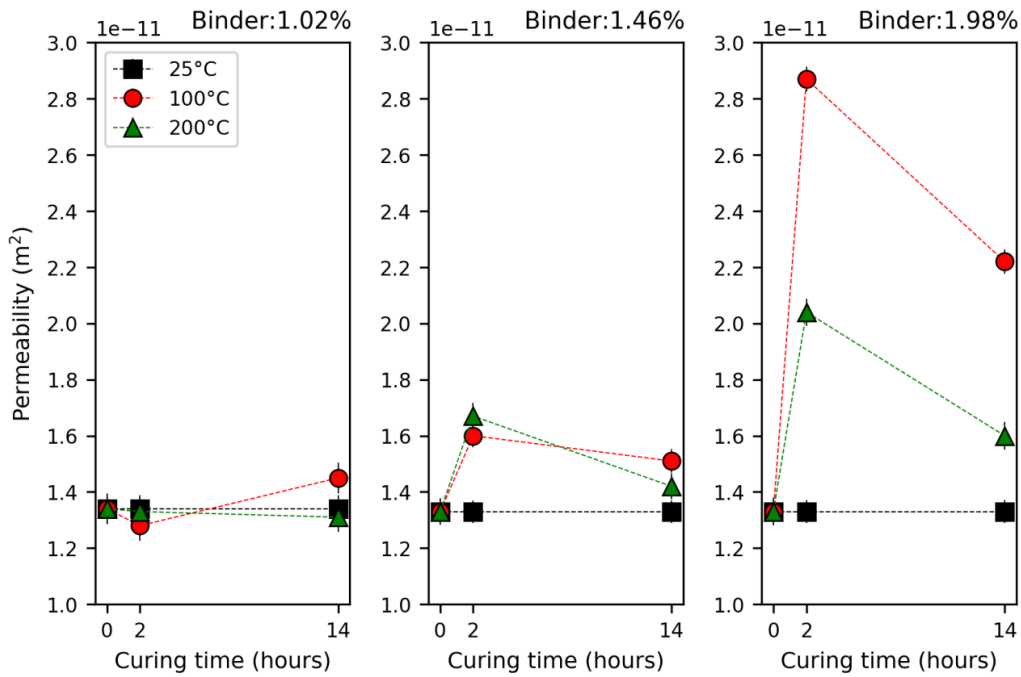
764

765 samples at 25°C.

766

Figure 11. Evaluation of the inertial effects for uncured samples at 25°C and a binder content

of 1.02%: (a) Darcy's law fit. Black symbols represent experimental measurements. The red

dashed line represents Darcy's law fit; (b) Forchheimer number at different flow rates**.**

770

771

Figure 12. Variation of permeability with binder content, curing temperature and time

773   **Table 1**. **Printing process parameters used with ExOne S-Print furan machine**

Average sand grain diameter	140 µm
American Foundry Society (AFS) number	97
Recoating speed	0.182 m/s (14%)
X Resolution	80 µm, 120 µm and 140 µm
Y Resolution	101.6 µm
Z-resolution/Layer thickness	280 µm
Print head voltage	78 V
Activator content(sulfonic acid)	0.18% of the weight of sand
Infrared heating temperature	32°C

774

775

776

777   **Table 2. Experimental parameters**

Parameters (Unit)	Category 1	Category 2	Category 3
Binder (wt%)	1.02±0.03	1.46±0.02	1.98±0.02
Curing time (hours)	2 and 14	2 and 14	2 and 14
Curing temperature (°C)	25, 100 and 200	25, 100 and 200	25, 100 and 200

778

779